

11/11/96  
11/11/96  
11/11/96  
63073

# **NUMERICAL SIMULATION OF FILM-COOLED ABLATIVE ROCKET NOZZLES**

## **Final Report**

**Contract No. NAG8-1097**

**Period: August 17, 1994 - April 15, 1996**

**Prepared For:  
NASA Marshall Space Flight Center  
Huntsville, Alabama 35812**

by

**D. B. Landrum and R. M. Beard**

**Propulsion Research Center  
Technical Report 96-002**

**The University of Alabama in Huntsville  
Huntsville, Alabama 35899  
(205) 890-7200**

**April 26, 1996**

## **FOREWORD**

This final report was submitted by the Propulsion Research Center of the University of Alabama in Huntsville upon the conclusion of contract NAG8-1097 with NASA Marshall Space Flight Center (MSFC) in Huntsville, Alabama. Responsibility for UAH program management and research tasks was held by the principal investigator, Dr. Brian Landrum. Dr. Landrum was assisted by UAH graduate research assistant R. M. Beard. The contents of this final report detail a numerical simulation to evaluate the impact of incorporating an additional coolant port downstream between the injector and nozzle throat in the NASA Fast Track chamber. The results of this study provide guidance in the development of a potentially lighter, second generation ablative rocket nozzle which maintains desired performance levels.

## TABLE OF CONTENTS

LIST OF FIGURES.....	iii
LIST OF TABLES.....	v
I. INTRODUCTION.....	1
II. NUMERICAL MODEL DEVELOPMENT.....	3
2.1. Modeling Approach.....	3
2.2. CFD Code.....	6
2.3. Nozzle Geometry and Boundary Conditions.....	7
2.4. Thermodynamic Properties of RP-1.....	8
2.5. Chemistry of LOX/RP-1.....	11
2.6. Viscosity of Added Species.....	12
2.7. Thermal Properties of Copper.....	16
2.8. Computational Grid.....	17
III. ANALYSIS RESULTS.....	21
3.1. Wall Temperature Distribution Comparison.....	21
3.2. Cracking of RP-1.....	23
3.3. Survivability of the Copper Lip.....	28
3.4. Performance Comparison.....	29
IV. Conclusions.....	30
V. Future Work.....	32
REFERENCES.....	33

## LIST OF FIGURES

<u>Figure</u>	<u>Page</u>
2.1 Baseline MSFC Fast Track Engine Chamber and Nozzle Geometry.....	4
2.2 Ablation Rate of Silica-Phenolic in a Reacting LOX/H <sub>2</sub> Environment.....	5
2.3 C <sub>p</sub> /R for C <sub>12</sub> H <sub>26</sub> and C <sub>12</sub> H <sub>24</sub> .....	8
2.4 H/RT for C <sub>12</sub> H <sub>26</sub> and C <sub>12</sub> H <sub>24</sub> .....	9
2.5 S/R for C <sub>12</sub> H <sub>26</sub> and C <sub>12</sub> H <sub>24</sub> .....	9
2.6 % Difference of C <sub>12</sub> H <sub>24</sub> from C <sub>12</sub> H <sub>26</sub> .....	10
2.7 Difference of H/RT between C <sub>12</sub> H <sub>24</sub> and C <sub>12</sub> H <sub>26</sub> .....	10
2.8 Viscosity of C <sub>2</sub> H <sub>2</sub> .....	14
2.9 Viscosity of C <sub>2</sub> H <sub>6</sub> .....	14
2.10 Viscosity of C <sub>6</sub> H <sub>6</sub> .....	15
2.11 Viscosity of RP-1.....	15
2.12 Thermal Conductivity of Pure Copper.....	16
2.13 Specific Heat of Pure Copper.....	17
2.14 Grid for No Film-Cooling and Injector Film-Cooling Cases (12,851 nodes).....	18
2.15 Grid for Injector and Downstream Port Film-Cooling Case (17,185 nodes).....	19
2.16 Close-up of Grid in the Region of the Copper Lip.....	19
2.17 Close-up of Grid in the Region of the Downstream Port.....	20
3.1 Nozzle Wall Temperature Distributions.....	22
3.2 RP-1 Mass Fractions for the Injector Film-Cooling Case.....	23
3.3 C <sub>6</sub> H <sub>6</sub> Mass Fractions for the Injector Film-Cooling Case.....	24
3.4 CH <sub>4</sub> Mass Fractions for the Injector Film-Cooling Case.....	24
3.5 RP-1 Mass Fractions at the Injector for the Downstream Port Film-Cooling Case.....	25
3.6 C <sub>6</sub> H <sub>6</sub> Mass Fractions at the Injector for the Downstream Port Film-Cooling Case.....	25

3.7 CH <sub>4</sub> Mass Fractions at the Injector for the Downstream Port Film-Cooling Case.....	26
3.8 RP-1 Mass Fractions at the Port for the Downstream Port Film-Cooling Case.....	27
3.9 C <sub>6</sub> H <sub>6</sub> Mass Fractions at the Port for the Downstream Port Film-Cooling Case.....	27
3.10 CH <sub>4</sub> Mass Fractions at the Port for the Downstream Port Film-Cooling Case.....	28
3.11 Temperature Distribution in the Copper Lip.....	29

## LIST OF TABLES

<b><u>Table</u></b>	<b><u>Page</u></b>
2.1 Mass Fraction Ranking of Potential Chemical Species.....	11
2.2 Summary of Viscosity Parameters for Added Species.....	13
3.1 Nozzle Performance Comparison.....	29

## I. INTRODUCTION

Historical and current NASA priorities include maintaining U.S. leadership in space exploration and commercial exploitation. Based on current economic realities, achieving this goal will require significant reductions in the cost and complexity of launch systems. To meet this need, NASA Marshall Space Flight Center (MSFC) has established a program to develop a low cost thrust chamber applicable to future upper-stage and booster systems in the 7K to 40K lbf thrust range, respectively. The current booster design parameters include:

- LOX/RP-1 propellants
- Up to 40K lbf thrust (avg)
- Chamber pressure of 400 psia (avg)
- Pressure-fed combustion chamber
- One restart capability

To help meet the requirement of low cost, the booster is planned to contain a relatively inexpensive replaceable ablative thrust chamber and nozzle. The eroded nozzle will be discarded after a mission. A new nozzle can then be bolted to the expensive turbomachinery which is reused.

MSFC has begun to develop a database for a first generation booster design by using its existing 12K lbf thrust "Fast Track" engine. To meet the design goals of system simplicity and low cost, the Fast Track chamber is made of a tape-wrapped silica phenolic liner. A major technical requirement of this approach is to achieve less than a 0.002 inch per second erosion rate with a maximum total film-cooling of 10% of the total fuel flowrate. Therefore, Fast Track program objectives include prediction of the ablative liner's erosion characteristics, ablation effects on engine performance, and to validate the erosion models in a hot-fire test program.

Preliminary predictions indicate that the low cost objective is obtainable. But a significant obstacle is excessive weight of the current system design due to the required thickness of the

ablative liner in the nozzle throat region where heat fluxes and thus ablation are significant. Minimization of the ablative liner thickness is also limited by the one restart requirement. Reduction of the heat flux to the liner in the throat could lead to a reduced composite wall thickness and thus reduced weight. Decreasing the throat ablation rate will also lead to less area ratio reduction and therefore more stable performance characteristics. These considerations suggest the potential need for a second generation thrust chamber with active cooling (film or transpiration) which minimizes the required thickness of the ablative liner in the throat region.

One method of reducing the throat ablation rate is to distribute the coolant more uniformly along the nozzle wall. The simplest way of achieving this is to divert a fraction of coolant from the injector face ports to a location along the nozzle wall between the injector and the throat. This approach should increase the extent of nozzle wall cooling by decreasing the amount of coolant capacity lost by diffusion of the coolant into the hot core exhaust flow. Also, the coolant flowrates at the injector and at the downstream port can be optimized to control the ablation along a larger fraction of the nozzle wall, allowing the ablative liner thickness to be minimized and thus minimizing the weight of the disposable rocket nozzle. But any scheme for modifying the wall coolant distribution must also include appropriate consideration of any adverse effects of injection on the flowfield and overall nozzle performance.

The objective of this research effort was to evaluate the impact of incorporating an additional coolant port downstream between the injector and nozzle throat in the NASA Fast Track chamber. The results of this study provide guidance in the development of a potentially lighter, second generation ablative rocket nozzle which maintains desired performance levels.



## II. NUMERICAL MODEL DEVELOPMENT

In this section, the development of a numerical model for the MSFC Fast Track engine is described. The particular topics addressed include (1) the modeling approach taken, (2) the capabilities of the Computational Fluid Dynamics (CFD) code that was used, (3) the determination and selection of the inputs to the analysis based upon the chosen modeling approach, and (4) the generation of the computational grids used in this study.

### 2.1. Modeling Approach

The baseline MSFC Fast Track engine simulated in this study has the following characteristics:

- Ablative silica-phenolic combustion chamber and nozzle
- Impinging injector design
- LOX/RP-1 propellants
- Nominal thrust of 12K lbf
- Chamber pressure of 300 psia (avg)
- Total oxidizer (LOX) flowrate of 33.19 lbm/sec
- Total fuel (RP-1) flowrate of 14.19 lbm/sec
- A maximum of 10% of total fuel flowrate used as film-coolant (1.42 lbm/sec)
- Overall mixture ratio of 2.34

The nozzle geometry, presented in Figure 2.1, has the following geometric characteristics:

- Throat diameter of 5.875 inches
- Contraction area ratio of 2.45
- Expansion area ratio of 2.19
- Overall chamber and nozzle length of 20.79 inches

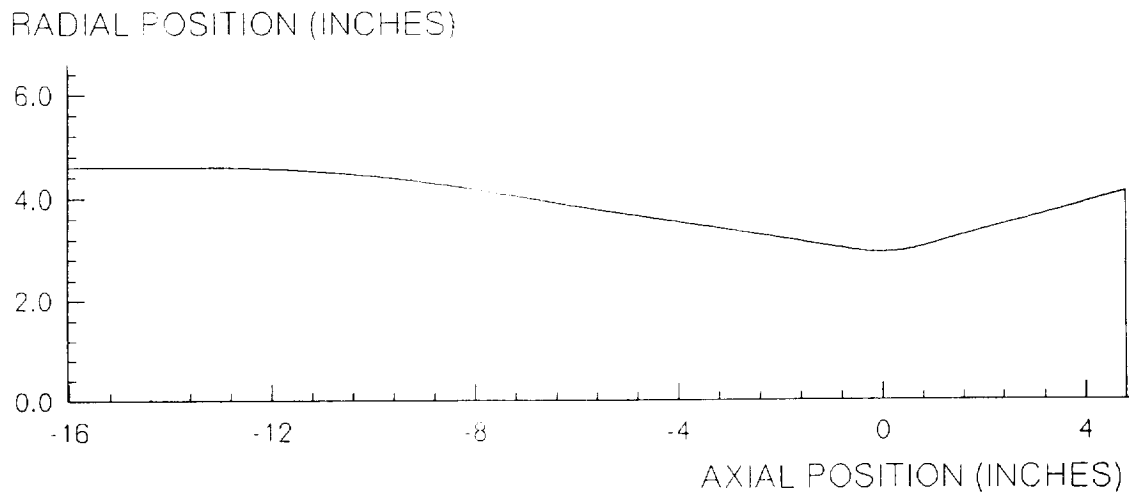


Figure 2.1: Baseline MSFC Fast Track Engine Chamber and Nozzle Geometry

The following modeling assumptions were made:

- 2-D axisymmetric flow
- Adiabatic nozzle wall
- Equilibrium chemistry
- Turbulent flow with a 7% inlet turbulence intensity
- Gaseous RP-1 coolant at room temperature (530°R)

A primary objective of this research was to hold the ablation rate of the silica-phenolic nozzle liner below 0.002 inch per second (2 mils/sec). Given the current state of CFD technology, a transient solution of the nozzle ablation is impossible. For this study, a nonablating adiabatic wall was assumed. Therefore, the simulation represents the initial steady-state nozzle wall temperature distribution. The only known ablation rate information for the silica-phenolic material comes from an Aerojet-General Corporation test in 1969 of a LOX/H<sub>2</sub> thrust chamber,<sup>1</sup> in which the erosion rate was measured as a function of chamber pressure and recovery temperature. This erosion rate data is presented in Figure 2.2. Assuming that the predicted

adiabatic wall temperature is equivalent to the recovery temperature, this data can be used to obtain an estimate of the initial ablation rate along the nozzle wall.

The ablation rate of silica-phenolic is expected to be higher in a LOX/RP-1 combustion environment than in a LOX/H<sub>2</sub> combustion environment. The ablation rate also increases with increasing chamber pressure. Therefore, the erosion rate curve for LOX/H<sub>2</sub> at 570 psia in Figure 2.2 was assumed to be a conservative approximation of the erosion rate curve for LOX/RP-1 at 300 psia. Based on this assumption, the recovery temperature must be kept below approximately 3800°R in order to keep the initial silica-phenolic erosion rate below 2 mils/sec. To provide a further margin of safety, the maximum recovery temperature threshold was set to an even lower 3600°R.

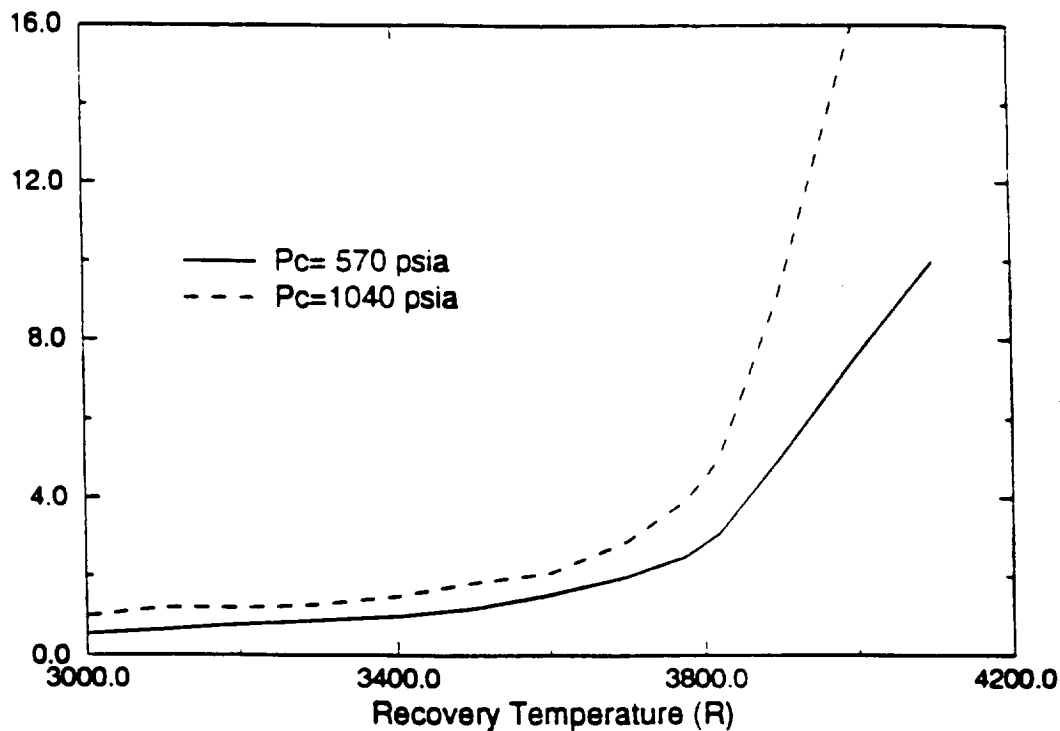


Figure 2.2: Ablation Rate of Silica-Phenolic in a Reacting LOX/H<sub>2</sub> Environment

Three basic cases were analyzed -- (1) no film-cooling, (2) diverting 10% of the total fuel flowrate as film-coolant at the injector face, and (3) diverting 5% of the total fuel flowrate as film-coolant at the injector face and another 5% as film-coolant at an additional coolant port located between the injector and throat. The predicted nozzle wall temperature distributions for these three cases were compared in order to draw some general conclusions about the effectiveness of film-cooling and its use in the control of the ablation rate of the silica-phenolic nozzle liner.

## 2.2. CFD Code

The numerical simulations presented in this report were made with the CFD-ACE code.<sup>2</sup> This is a commercial code developed by CFD Research Corporation in Huntsville, Alabama. The code uses a pressure-based finite-volume approach to solve the Favre-averaged Navier-Stokes equations for laminar or turbulent, incompressible or compressible, reacting or non-reacting, steady-state or transient flows. Cartesian or body-fitted grids for 2-D planar, 2-D axisymmetric, and 3-D flows with multiple inlets, outlets, and internal blockages can be modeled. An implicit iterative scheme is used to solve steady-state problems and various upwind and central spatial discretization schemes can be chosen. SIMPLEC or the non-iterative PISO scheme are used for the pressure-velocity coupling. Chemistry options include equilibrium, single-step, and multi-step finite rate kinetics. Various turbulence model options (mixing length, k- $\epsilon$ , RNG, etc.) are also available. For physical models, the code has a built-in database of JANNAF property tables for a limited number of gaseous species. The Lennard-Jones Model or Sutherland's Law is used in the determination of molecular viscosity. The code includes other physical models for natural and forced convection, radiative heat transfer, conjugate gradient heat transfer, thermodynamic processes, and mass transfer with multicomponent diffusion. The code is user-friendly with a graphical user interface for (1) creating the geometry and grid, (2) creating the CFD model, and (3) viewing the resulting solution.

### 2.3. Nozzle Geometry and Boundary Conditions

A schematic of the baseline combustion chamber and nozzle geometry provided by NASA MSFC was shown in Figure 2.1. A chamber pressure of 300 psia and a core chamber temperature of 6295°R were assumed. All nozzle inflow properties were considered uniform and were held constant. The nozzle exit was modeled as a supersonic outlet, and the nozzle wall was assumed to be adiabatic. Turbulent flow was assumed at all inlets with a 7% turbulence intensity. Recognizing the current limitations in modeling turbulent compressible flows, CFD Research Corp. recommended using the standard k- $\epsilon$  turbulence model.

The gaseous RP-1 coolant temperature was assumed to be 530°R. Gaseous RP-1 coolant was selected since the phase change behavior of RP-1 was unknown. Ignoring the heat absorbed by the coolant during the phase change simplified the analysis and also produced conservative predictions of wall cooling requirements. The coolant port was modeled as a circumferential slot next to the chamber wall. The slot area was estimated so that the gaseous RP-1 momentum would match the actual liquid RP-1 momentum.

The combustion of LOX with RP-1 is extremely complicated with over 100 possible reaction steps identified to date. Therefore, the analysis was simplified by modeling the chemistry of LOX/RP-1 as equilibrium throughout the nozzle. This choice should result in the maximum core flow and nozzle wall temperatures and thus represents a worst-case scenario for the extent of nozzle wall cooling.

The selection of the location and geometry of the additional coolant port was arbitrary and is only intended to provide a general idea of the effects of port geometry and location on the optimization of film-cooling of the nozzle wall. The downstream injection port was modeled as a 0.0135 inch wide annular coolant passageway with an inner, annular copper lip. The copper lip was 0.049 inches thick and 1 inch long. The port was located halfway between the injector face and throat (8 inches from the throat). Copper was chosen as the lip material since it is relatively inexpensive and has a relatively high thermal conductivity. Thus, another primary study objective was to determine if the flow of coolant would be sufficient to keep the copper lip from melting.

The CFD-ACE conjugate gradient heat transfer model was used to model the heat conduction in the copper lip.

#### 2.4. Thermodynamic Properties of RP-1

RP-1 is a complex mixture consisting primarily of dodecane ( $C_{12}H_{26}$ ) with various other smaller molecule hydrocarbons. The overall average composition of RP-1 is assumed to be  $C_nH_{1.94n}$ , with  $n \approx 12$ . Initially, dodecane ( $C_{12}H_{26}$ ) was chosen to model RP-1. However, after discussions with NASA MSFC, dodecene ( $C_{12}H_{24}$ ) was chosen since it provides an overall mixture composition and molecular weight closer to that of RP-1<sup>3</sup>. To evaluate the effects of this assumption, the JANNAF thermodynamic property curvefit data for gaseous dodecane and dodecene were plotted and compared. Figures 2.3, 2.4, and 2.5 are plots of  $C_p/R$ ,  $H/RT$ , and  $S/R$ , respectively, for gaseous  $C_{12}H_{26}$  and  $C_{12}H_{24}$ . Figures 2.6 and 2.7 show the difference in these properties for the two hydrocarbons. As can be seen from these figures, the thermodynamic properties of gaseous dodecane and dodecene are very similar. Therefore, gaseous dodecene ( $C_{12}H_{24}$ ) reasonably models gaseous RP-1.

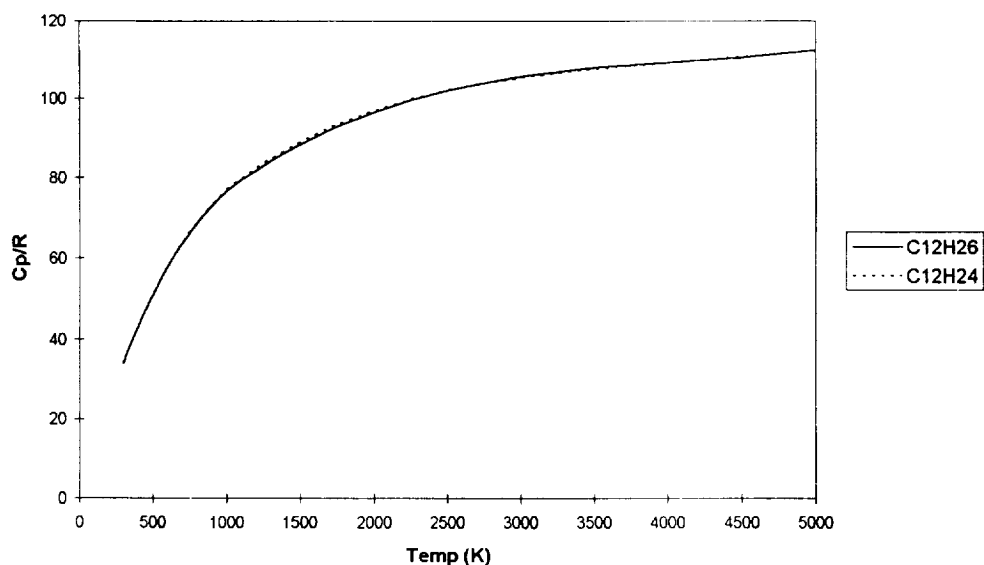


Figure 2.3:  $C_p/R$  for  $C_{12}H_{26}$  and  $C_{12}H_{24}$

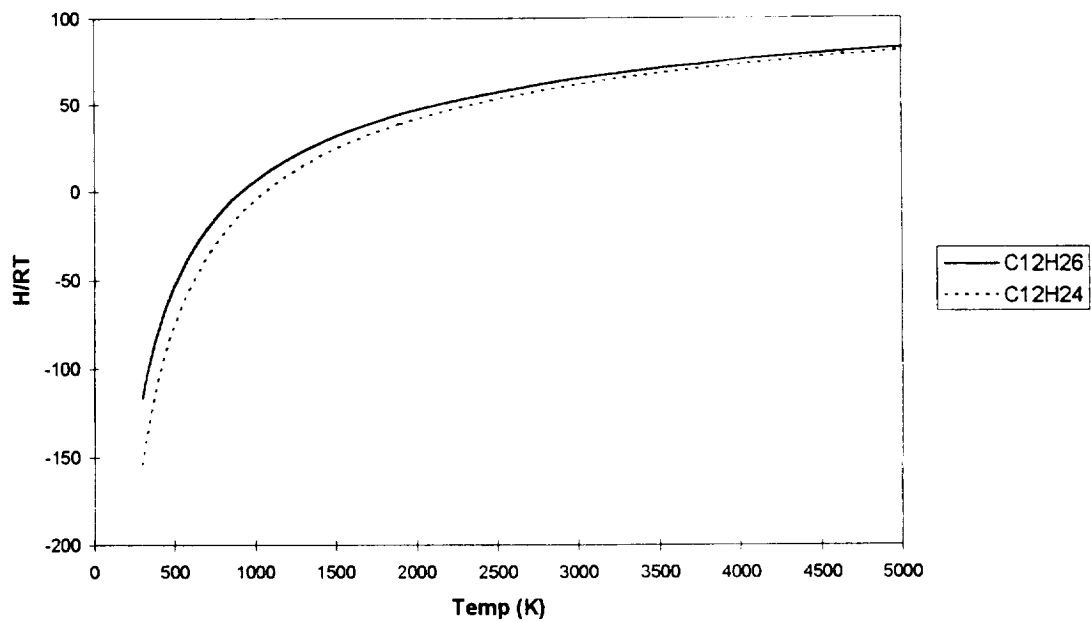


Figure 2.4:  $H/RT$  for  $C_{12}H_{26}$  and  $C_{12}H_{24}$

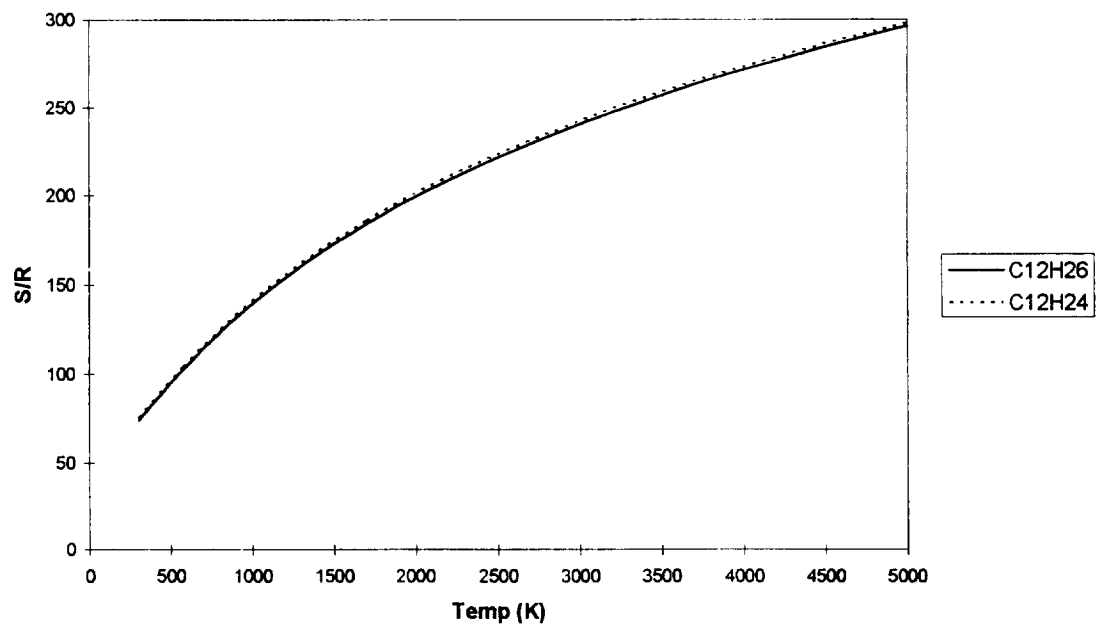


Figure 2.5:  $S/R$  for  $C_{12}H_{26}$  and  $C_{12}H_{24}$

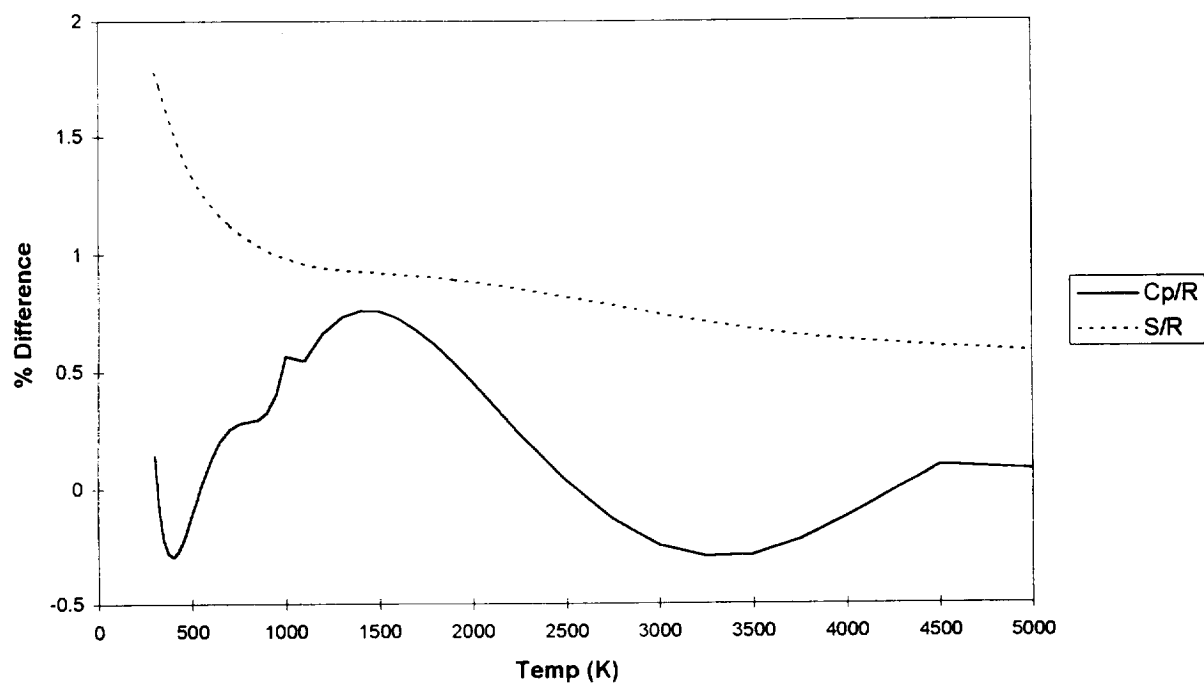


Figure 2.6: % Difference of  $C_{12}H_{24}$  from  $C_{12}H_{26}$

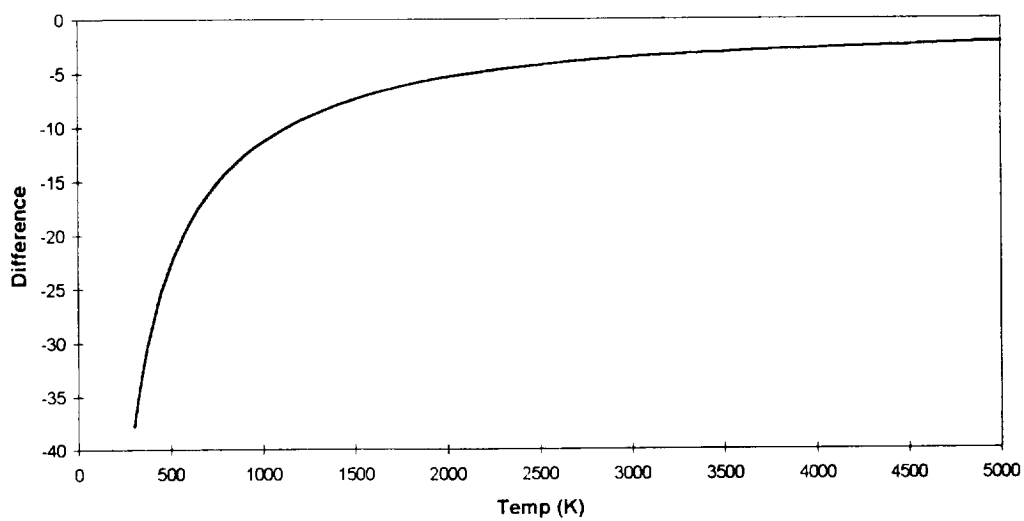


Figure 2.7: Difference of  $H/RT$  between  $C_{12}H_{24}$  and  $C_{12}H_{26}$



## 2.5. Chemistry of LOX/RP-1

Another important modeling issue that had to be addressed was which chemical species to include in the calculation of the chemical equilibrium state of LOX/RP-1. To address this issue, the Thermodynamic Equilibrium Program (TEP) was used to conduct a parametric study of the relative importance of potential chemical species arising in the calculation of the LOX/RP-1 chemical equilibrium state over a range of temperatures and mixture (O/F) ratios.<sup>4</sup> The mixture ratio was varied from 0.0 to 2.0 and the temperature from 300 K to 3500 K. All of the species, excluding condensed species, were ranked by the maximum mass fraction of each present over the entire temperature and O/F range. Table 2.1 shows this ranking of the potential chemical species.

Table 2.1: Mass Fraction Ranking of Potential Chemical Species

Max. Mass Fraction Above 1.0%	Max. Mass Fraction From 0.1% to 1.0%	Max. Mass Fraction From 0.01% to 0.1%	Max. Mass Fraction Below 0.01%
C <sub>12</sub> H <sub>24</sub>	C <sub>2</sub> H <sub>6</sub>	HO <sub>2</sub>	HCO
CO	C <sub>3</sub> H <sub>6</sub>	CH <sub>2</sub>	H <sub>2</sub> O <sub>2</sub>
H <sub>2</sub> O	C <sub>2</sub> H	C <sub>3</sub>	CH <sub>2</sub> O <sub>2</sub>
CO <sub>2</sub>	CH <sub>3</sub>	C <sub>2</sub> H <sub>3</sub>	CH <sub>2</sub> O
H <sub>2</sub>		C <sub>6</sub> H <sub>5</sub>	C
OH			CH
H			C <sub>2</sub>
O <sub>2</sub>			C <sub>2</sub> O
O			C <sub>2</sub> H <sub>5</sub>
CH <sub>4</sub>			C <sub>3</sub> H <sub>8</sub>
C <sub>2</sub> H <sub>2</sub>			I-C <sub>4</sub> H <sub>10</sub>
C <sub>6</sub> H <sub>6</sub>			C <sub>5</sub>
C <sub>2</sub> H <sub>4</sub>			N-C <sub>4</sub> H <sub>10</sub>

Based on Table 2.1, for the calculation of chemical equilibrium of LOX/RP-1, only those chemical species which attained a maximum mass fraction of at least 0.1% in the parametric study were included in the subsequent film-cooling simulations. However, after running the first film-cooling simulation (injector face only), three species which met the above criteria did not attain mass fractions of at least 0.1% in the simulation --  $C_3H_6$ ,  $C_2H$ , and  $CH_3$ . Therefore, these species were also neglected in the chemical equilibrium calculation. Thus, fourteen species were included in the final calculation of chemical equilibrium of LOX/RP-1:  $C_{12}H_{24}$ , CO,  $H_2O$ ,  $CO_2$ ,  $H_2$ , OH, H,  $O_2$ , O,  $CH_4$ ,  $C_2H_2$ ,  $C_6H_6$ ,  $C_2H_4$ , and  $C_2H_6$ . CFD-ACE has a built-in JANNAF thermodynamic property database for all of these species except for  $C_{12}H_{24}$ ,  $C_2H_2$ ,  $C_6H_6$ , and  $C_2H_6$ . JANNAF thermodynamic property data for these species were obtained from the TEP code and other reference texts.

## 2.6. Viscosity of Added Species

Viscosity data for the four added species ( $C_{12}H_{24}$ ,  $C_2H_2$ ,  $C_6H_6$ , and  $C_2H_6$ ) also had to be determined. CFD-ACE assumes viscosity is modeled by either the Lennard-Jones model:

$$\mu = 2.6693 \times 10^{-6} \frac{\sqrt{M \cdot T}}{\sigma^2 \cdot \Omega_\mu}, \quad (1)$$

where  $\mu$  is in  $[kg/(m \cdot s)]$ ,  $T$  is in  $[K]$ ,  $M$  is the molecular weight,  $\sigma$  is in  $[Å]$ , and  $\Omega_\mu$  is a tabulated function of  $\kappa T/\epsilon$ ; or by Sutherland's Law:

$$\mu = \frac{A \cdot T^{\frac{1}{2}}}{(B + T)}, \quad (2)$$

where  $T$  is in  $[K]$  and  $\mu$  is in  $[kg/(m \cdot s)]$ . The Lennard-Jones viscosity parameters ( $\sigma$  and  $\epsilon/\kappa$ ) for  $C_2H_2$ ,  $C_6H_6$ , and  $C_2H_6$  were obtained from a NASA technical report.<sup>5</sup> The Lennard-Jones viscosity parameters for  $C_{12}H_{24}$  were estimated from the critical pressure and critical temperature

of RP-1 by using the method of Bird, Stewart, and Lightfoot.<sup>6</sup> The critical pressure and critical temperature of RP-1 were obtained from CPIA data.<sup>7</sup> Modeling viscosity by the Lennard-Jones model in the CFD-ACE code involves a table-lookup every time that a viscosity is required. The Sutherland's Law model is a relatively quick, explicit one-step calculation, and therefore was chosen to model viscosity for every species included in the model. The Lennard-Jones viscosity parameters determined for  $C_{12}H_{24}$ ,  $C_2H_2$ ,  $C_6H_6$ , and  $C_2H_6$  were used to generate a curvefit to Sutherland's Law for each of the four species. Table 2.2 provides a summary of the Lennard-Jones and Sutherland's Law viscosity parameters for the four species. Figures 2.8, 2.9, 2.10, and 2.11 are plots of the viscosity of  $C_2H_2$ ,  $C_2H_6$ ,  $C_6H_6$ , and  $C_{12}H_{24}$ , respectively, calculated by the Lennard-Jones model, the Sutherland's Law curvefit, and some limited low temperature experimental data from a viscosity handbook.<sup>8</sup> Comparing the various plots, it is obvious that Sutherland's Law provides a reasonable estimate of the viscosities of  $C_2H_2$ ,  $C_2H_6$ ,  $C_6H_6$ , and  $C_{12}H_{24}$ .

Table 2.2: Summary of Viscosity Parameters for Added Species

Added Species	Lennard-Jones Model		Sutherland's Law	
	$\sigma$ (Å)	$\epsilon/\kappa$ (K)	A	B
$C_2H_2$	4.033	231.8	1.1590E-6	303.34
$C_2H_6$	4.443	215.7	1.0242E-6	279.14
$C_6H_6$	5.349	412.3	1.0997E-6	473.10
$C_{12}H_{24}$	7.53	523	8.0724E-7	584.12

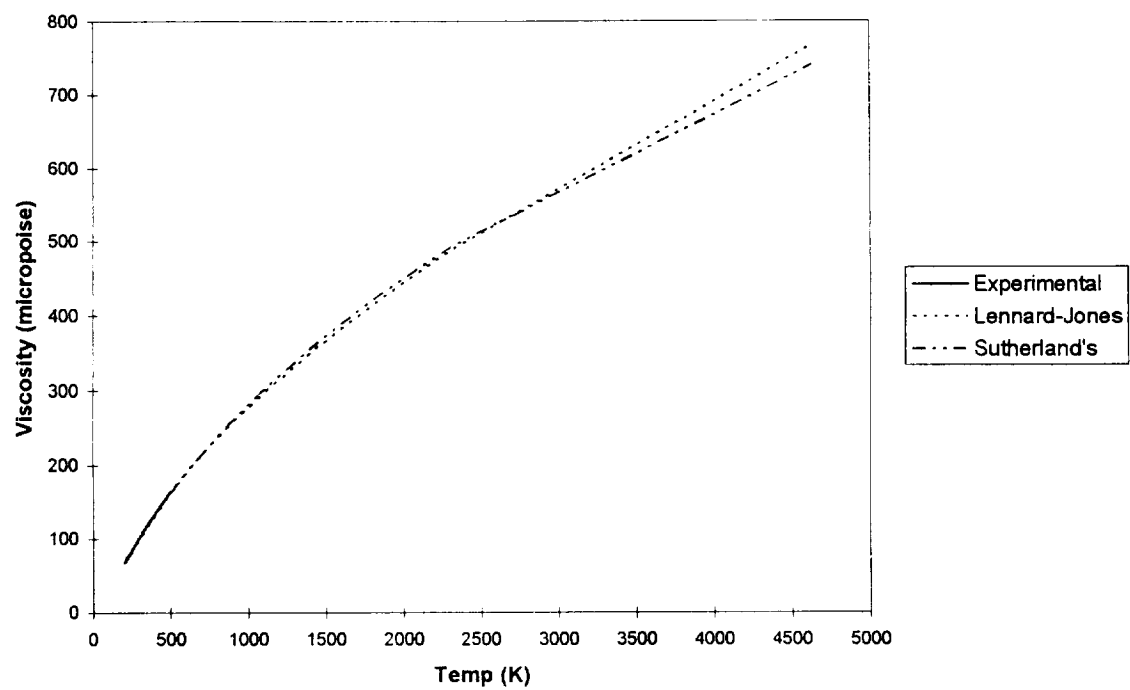


Figure 2.8: Viscosity of C<sub>2</sub>H<sub>2</sub>

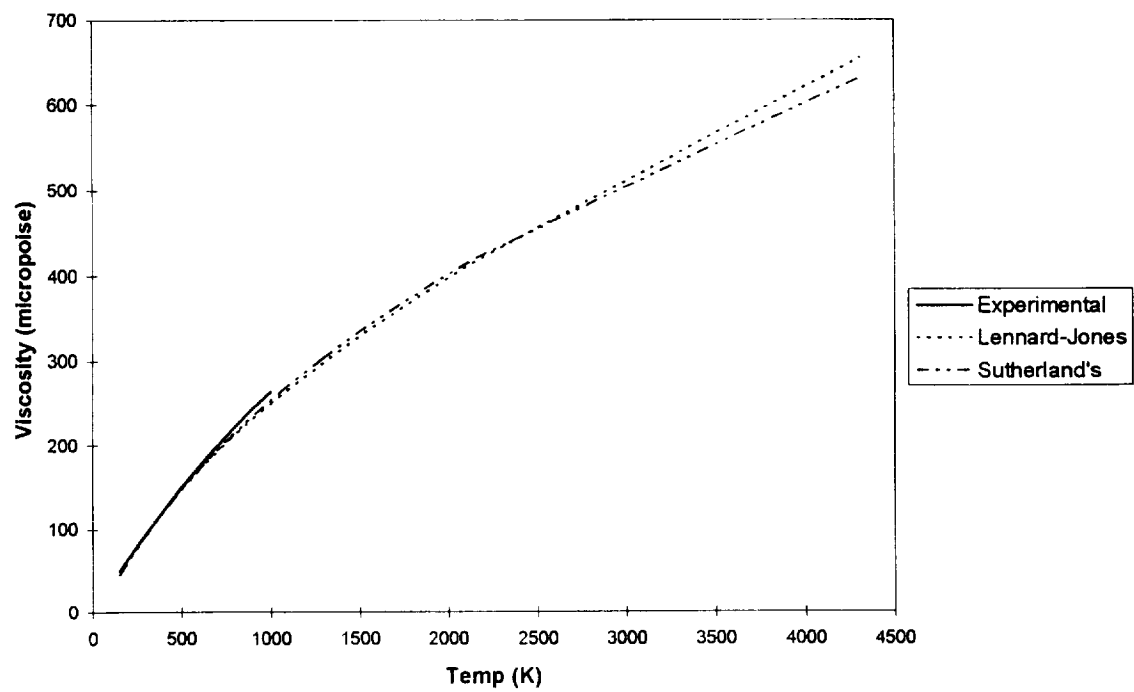


Figure 2.9: Viscosity of C<sub>2</sub>H<sub>6</sub>

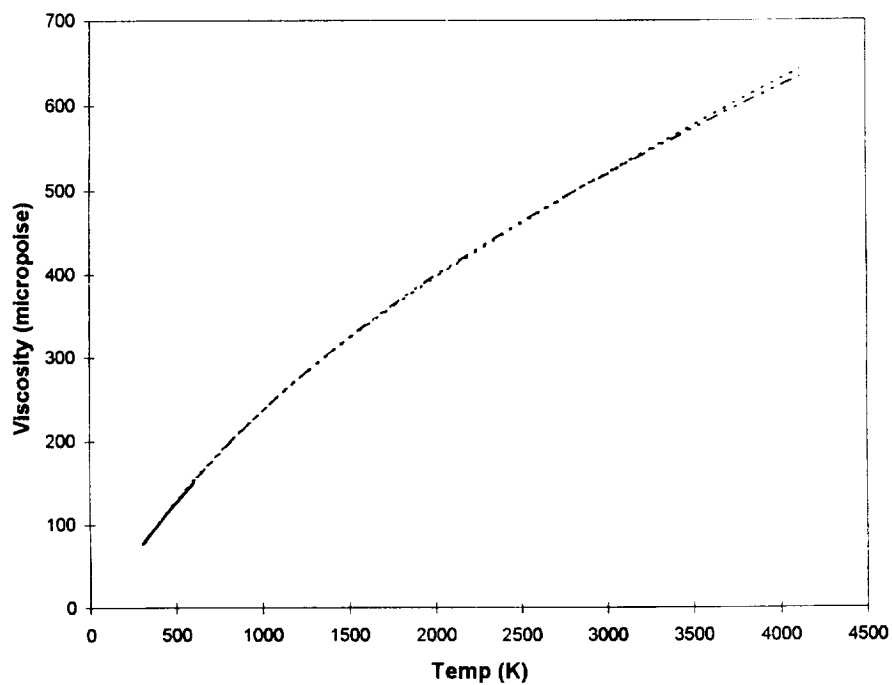


Figure 2.10: Viscosity of C<sub>6</sub>H<sub>6</sub>

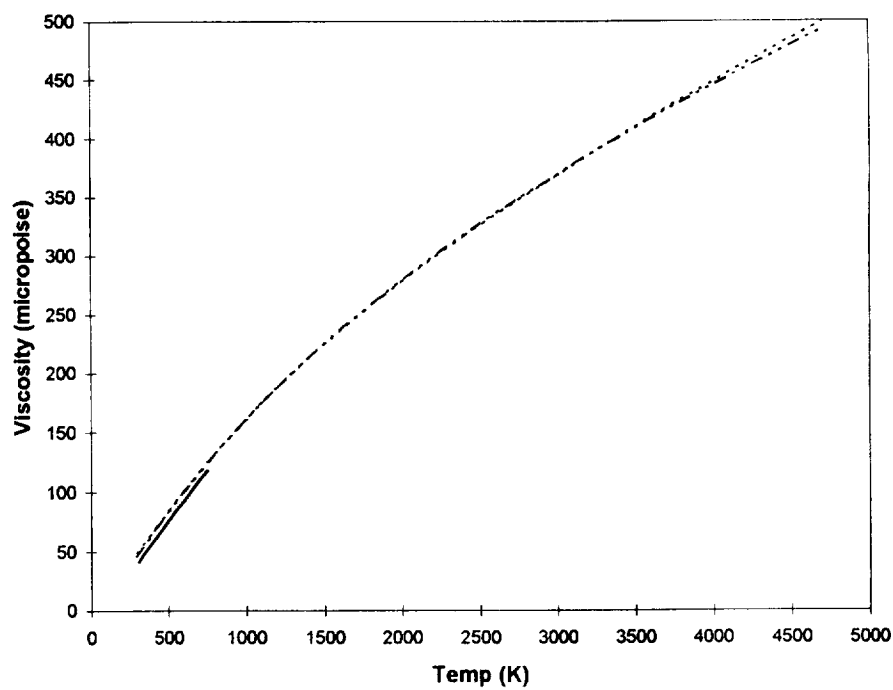


Figure 2.11: Viscosity of RP-1

## 2.7. Thermal Properties of Copper

The numerical simulation also required models for the thermal conductivity and specific heat of copper. The CFD-ACE conjugate gradient heat transfer model allows input of up to fifth-order polynomial curvefits for these parameters as a function of temperature. Experimental data for the thermal conductivity and specific heat of pure copper over a temperature range of 100 K to 1200 K were obtained from Ref. 9. Since these thermal properties varied almost linearly with only a slight amount of curvature over the 200 K to 1200 K temperature range of interest in this study, only a quadratic polynomial curvefit was developed. The experimental and curvefit values of thermal conductivity and specific heat over the temperature range of interest are compared in Figures 2.12 and 2.13, respectively. The quadratic polynomial curvefits provide reasonable estimates.

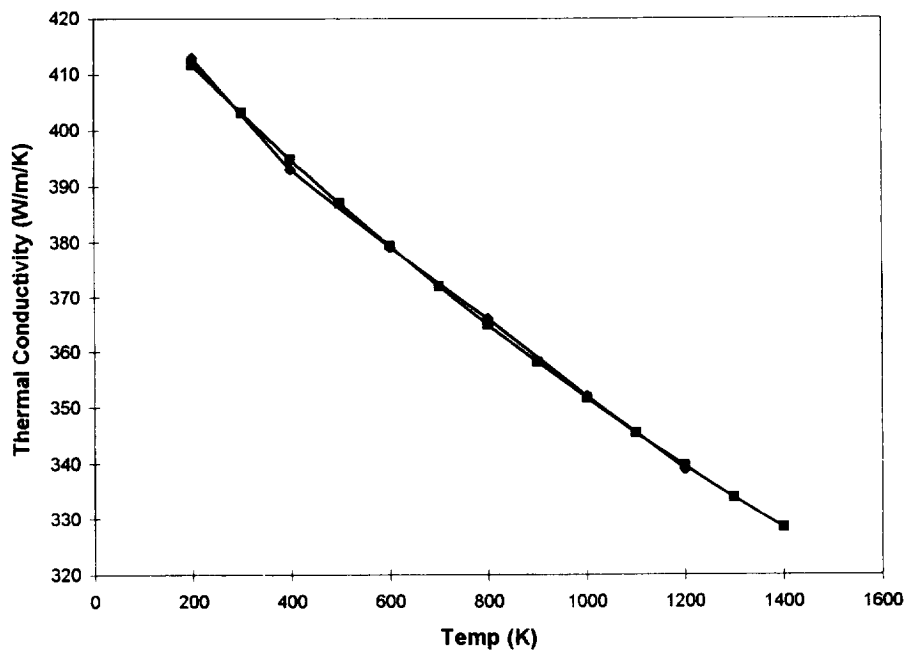


Figure 2.12: Thermal Conductivity of Pure Copper

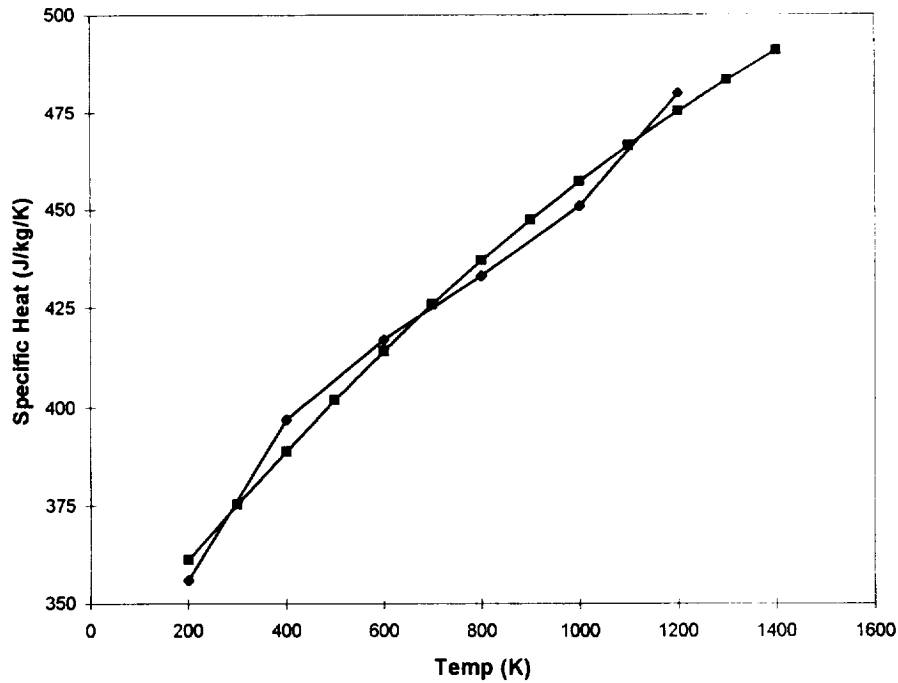


Figure 2.13: Specific Heat of Pure Copper

## 2.8. Computational Grid

The final modeling issue that had to be addressed was the computational grid. Two grids were generated -- one grid for the no film-cooling and injector film-cooling simulations, and the other grid for the injector and downstream port film-cooling simulation. These computational grids are shown in Figures 2.14 and 2.15. The throat is located at an axial position of  $X=0$ . Both grids employed grid clustering (exponential stretching) at the nozzle wall and throat in order to better model these high gradient regions of the flowfield. The injector face coolant inlet had 11 computational nodes across the slot width in order to resolve this important region of the flowfield. The significant increase in nodes for the downstream port film-cooling simulation was due to the fact that additional nodes in the radial direction had to be added in order to adequately model the downstream port coolant passageway and the copper lip. As before, the grid for the

downstream port coolant passageway was designed so that it had 11 nodes across its width. The grid for the copper lip had 20 nodes defining its width, mainly as a result of the need for smooth radial grid spacing transitions between the two radial regions of highest grid clustering. Figure 2.16 provides a close-up view of the grid in the region of the copper lip. The copper lip extends one inch in the axial direction from an axial position of -9 inches to an axial position of -8 inches. The two dark regions in Figure 2.16 are the two radial regions of highest grid clustering -- the downstream coolant port passageway next to the nozzle wall, and the region next to the displaced part of the nozzle wall and the copper lip. Figure 2.17 provides a close-up view of the grid in the region of the downstream port and demonstrates the smooth radial grid spacing transitions made in this region.

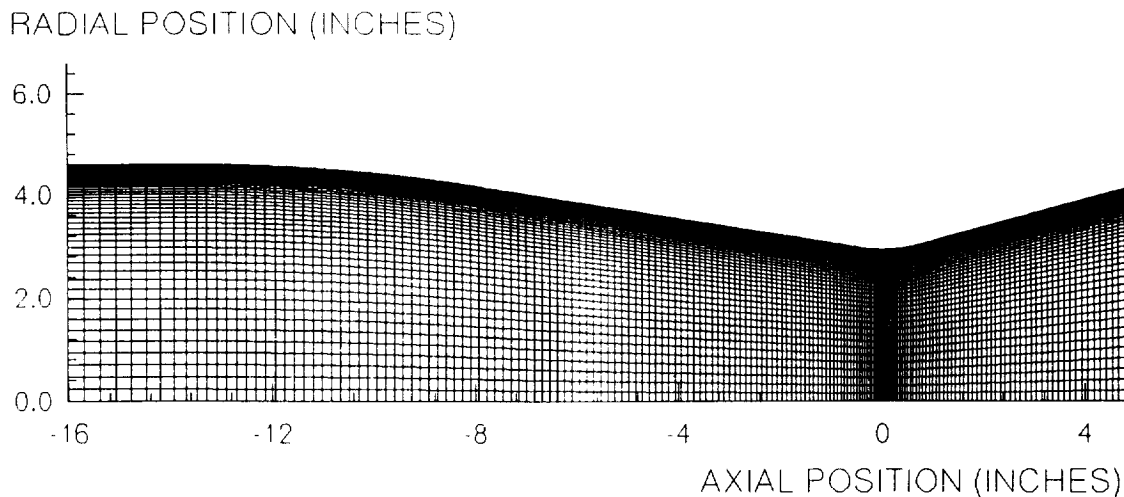


Figure 2.14: Grid for No Film-Cooling and Injector Film-Cooling Cases (12,851 nodes)



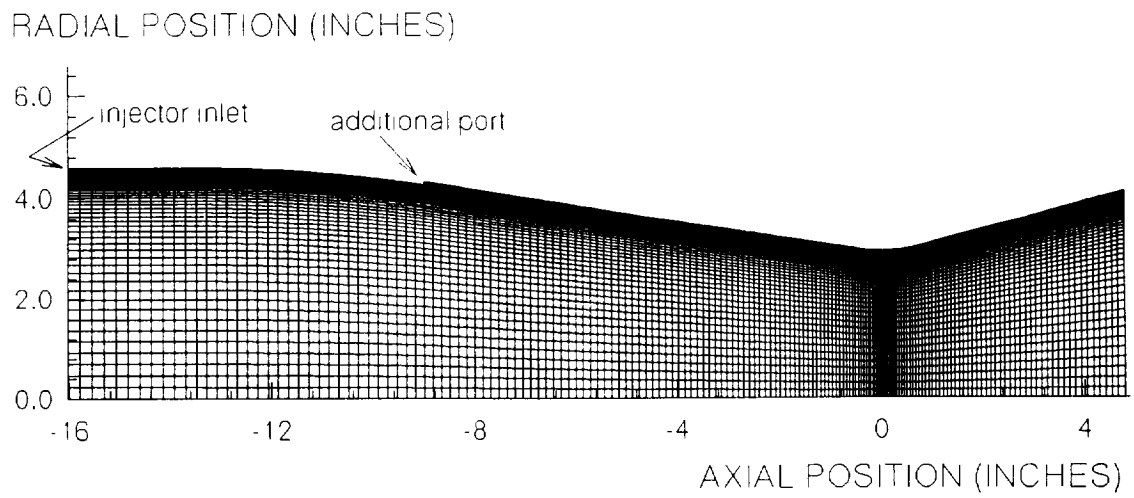


Figure 2.15: Grid for Injector and Downstream Port Film-Cooling Case (17,185 nodes)

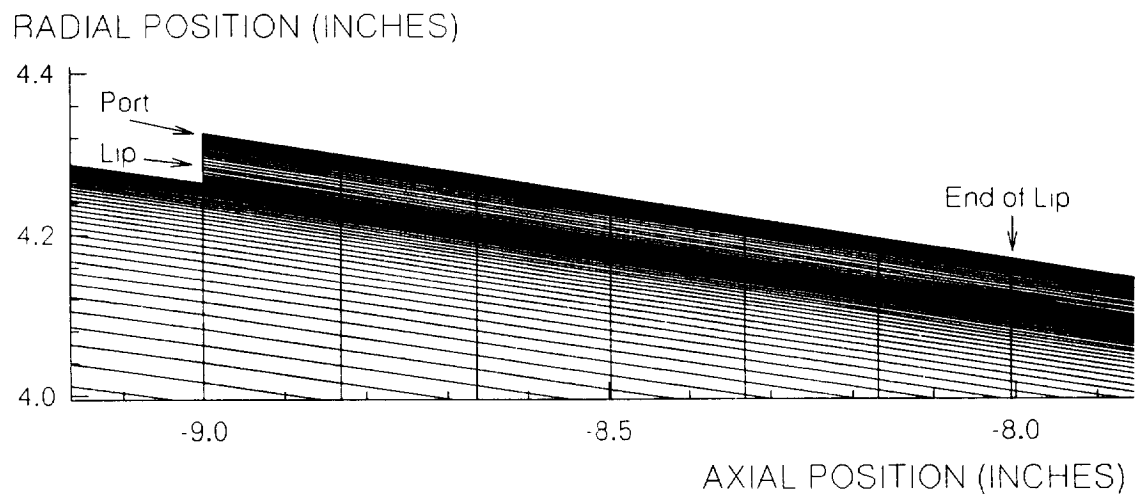


Figure 2.16: Close-up of Grid in the Region of the Copper Lip

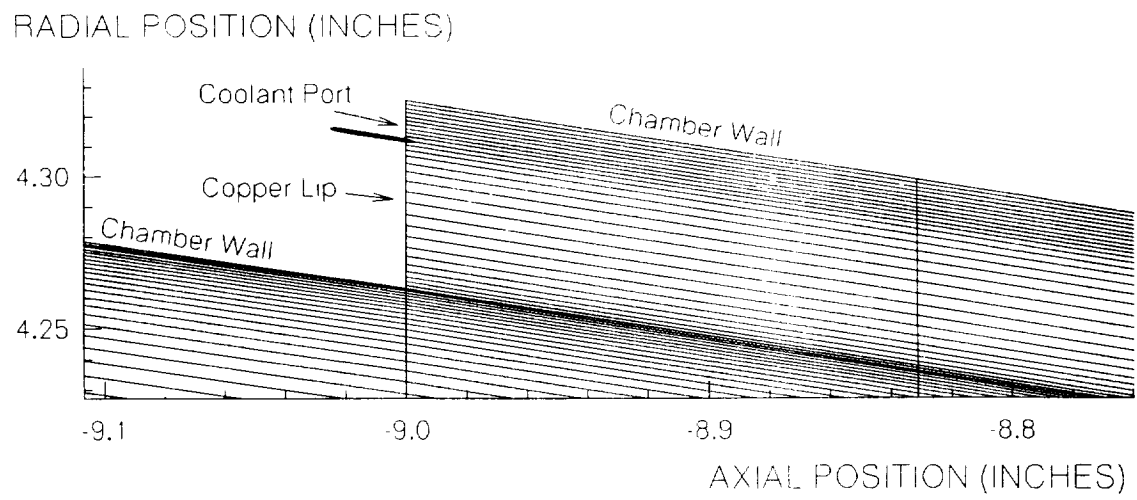


Figure 2.17: Close-up of Grid in the Region of the Downstream Port

### III. ANALYSIS RESULTS

The three cases simulated in this study were: (1) no film-cooling, (2) diversion of 10% of the total fuel flowrate as film-coolant at the injector face, and (3) diversion of 5% of the total fuel flowrate as film-coolant at the injector and another 5% as film-coolant at the additional coolant port downstream of the injector. In this chapter, the numerical analysis results for these cases are presented. In particular, this discussion focuses on (1) the nozzle wall temperature distribution comparison for the three cases simulated, (2) the breakdown of RP-1 coolant and its effect on the extent of film-cooling along the nozzle wall, (3) the survivability of the copper lip in the hot gas environment, and (4) the performance comparison for the three cases simulated.

#### 3.1. Wall Temperature Distribution Comparison

Figure 3.1 is a comparative plot of the nozzle wall temperature distributions for the three cases simulated. Based on the Aerojet ablation data, a maximum wall temperature of 3600°R is allowed for maintaining the ablation rate of the nozzle liner below 2 mils/sec (dotted line on plot). Without film-cooling, the chamber wall temperature is almost constant at 6200°R. The wall only cools slightly as the flow expands through the throat. These temperature levels would correlate to significant initial ablation rates. Diverting 10% of the fuel flowrate for film-cooling at the injector face drops the nozzle wall temperatures dramatically from the temperatures that would be experienced if no film-cooling were used. However, just ahead of the throat, the nozzle wall temperature for the injector film-cooling case begins to exceed the 3600°R threshold temperature.

By diverting half of the film-coolant to the downstream coolant port, the nozzle wall temperature in the throat region is maintained well below the 3600°R threshold temperature. However, a one inch section of nozzle wall immediately upstream of the additional coolant port exceeds the 3600°R threshold, due to the decrease in injector face coolant. The drastic drop in wall temperature at an axial location of -9 inches is due to the fact that the ablative nozzle wall at

that location is displaced and is adjacent to the coolant passageway of the additional coolant port. These results suggest that a more optimum distribution of film-coolant between the two coolant ports (possibly 6% of the fuel flowrate to the injector and 4% of the fuel flowrate to the additional coolant port) would bring the entire nozzle wall temperature distribution down below the 3600°R threshold temperature. Figure 3.1 also indicates that simply adding slightly more coolant massflow at the injector face could possibly drop the wall temperature to acceptable levels. Since the additional throat coolant port would significantly increase the complexity and cost of the nozzle design, increased injector coolant massflow might be the best alternative. But this approach must also consider the impact of the increase in coolant flowrate on overall system performance.

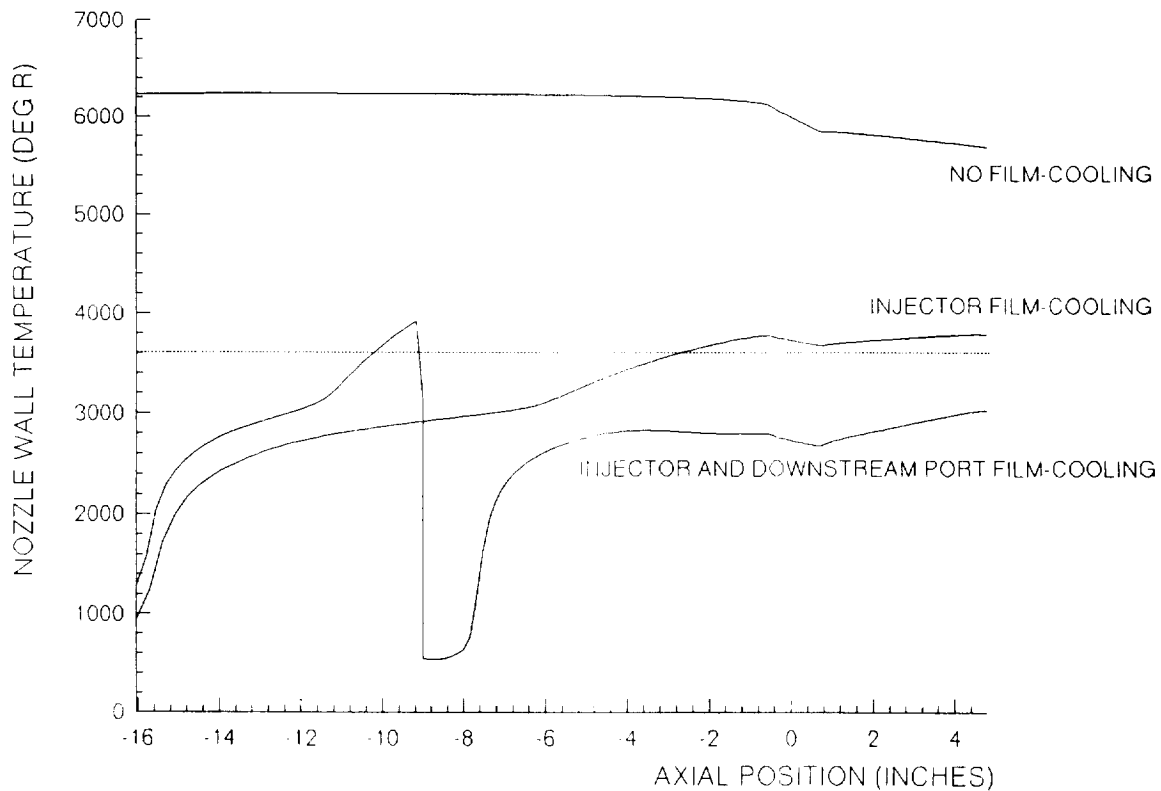


Figure 3.1: Nozzle Wall Temperature Distributions

### 3.2. Cracking of RP-1

As the injectant moves along the nozzle wall, thermal energy from the hot gas core causes the RP-1 to crack into smaller hydrocarbons. Thus, the cooling effectiveness of RP-1 is primarily due to the highly endothermic chemical reactions that occur during the cracking process. Since the chemistry was modeled as equilibrium, the cracking of RP-1 results predominantly in the formation of benzene ( $C_6H_6$ ). Benzene subsequently cracks into smaller hydrocarbons, primarily methane ( $CH_4$ ). Oxygen and oxygen-containing molecules from the core flow diffuse into the coolant layer and react with methane to form carbon monoxide (CO) and later carbon dioxide ( $CO_2$ ). At this point, the coolant effectiveness is reduced.

Figures 3.2, 3.3, and 3.4 are contour plots of the mass fractions of RP-1,  $C_6H_6$ , and  $CH_4$ , respectively, for the injector film-cooling case. These three plots illustrate the cracking process for RP-1 under equilibrium conditions. RP-1 quickly breaks down during the first 0.6 inches (Figure 3.2). A significant fraction of benzene exists much further along the wall to an axial position of -11.6 inches (Figure 3.3). Figure 3.4 shows that the reach of methane extends to an axial position of approximately -6 inches. As shown in the nozzle wall temperature distribution for film-cooling at the injector face (Figure 3.1), a significant increase in the axial temperature

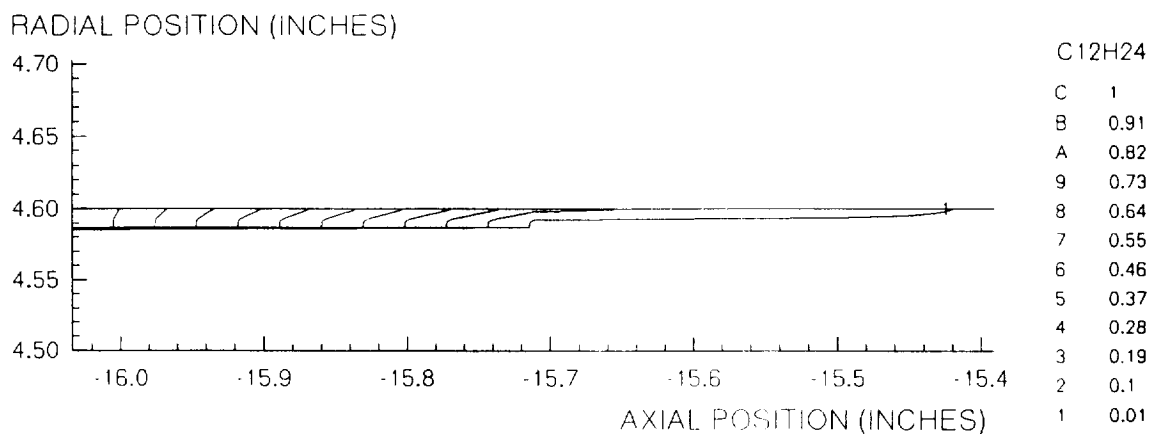


Figure 3.2: RP-1 Mass Fractions for the Injector Film-Cooling Case

gradient along the nozzle wall occurs at an axial position of -6 inches. These trends appear to correlate with the assumption that the cooling effectiveness of RP-1 is primarily due to the highly endothermic cracking process.

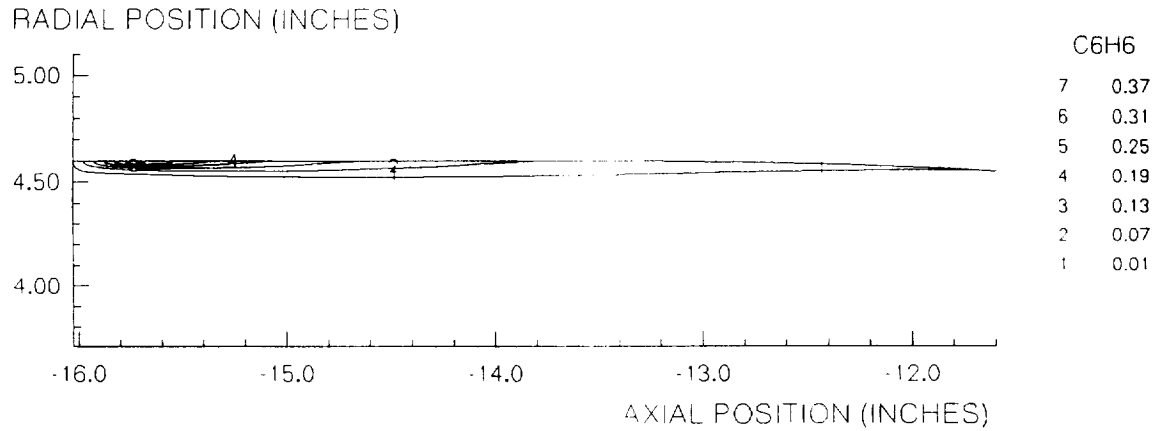


Figure 3.3:  $C_6H_6$  Mass Fractions for the Injector Film-Cooling Case

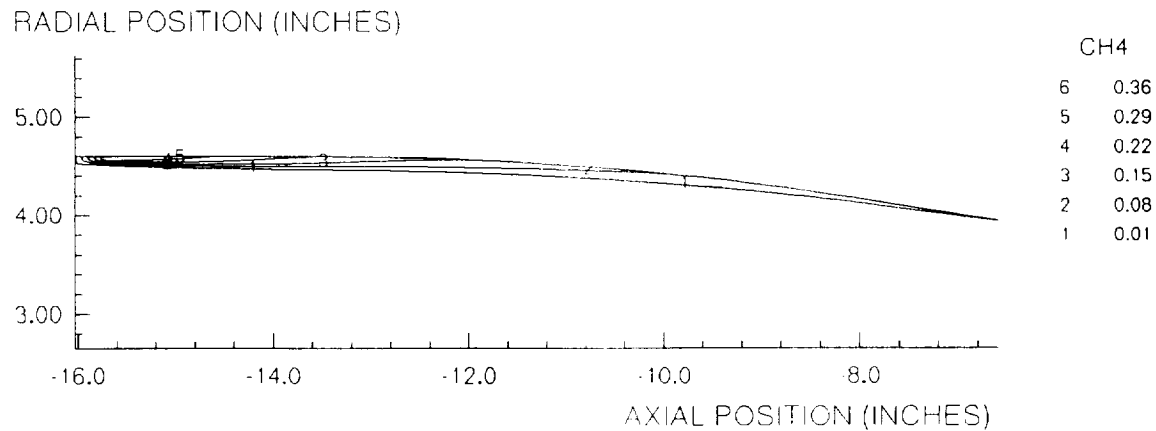


Figure 3.4:  $CH_4$  Mass Fractions for the Injector Film-Cooling Case

Figures 3.5, 3.6, and 3.7 are contour plots of the mass fractions of RP-1,  $C_6H_6$ , and  $CH_4$ , respectively, at the injector for case 3 (injector and downstream port film-cooling). These plots also illustrate the cracking process for RP-1 under equilibrium conditions. Due to the reduced coolant flowrate, the gaseous RP-1 quickly breaks down in the first 0.2 inches past the injector

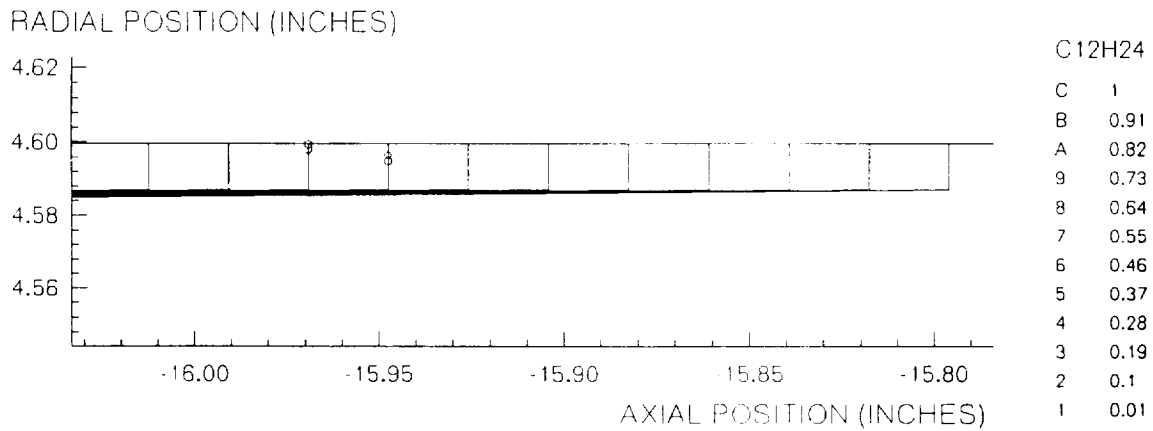


Figure 3.5: RP-1 Mass Fractions at the Injector for the Downstream Port Film-Cooling Case

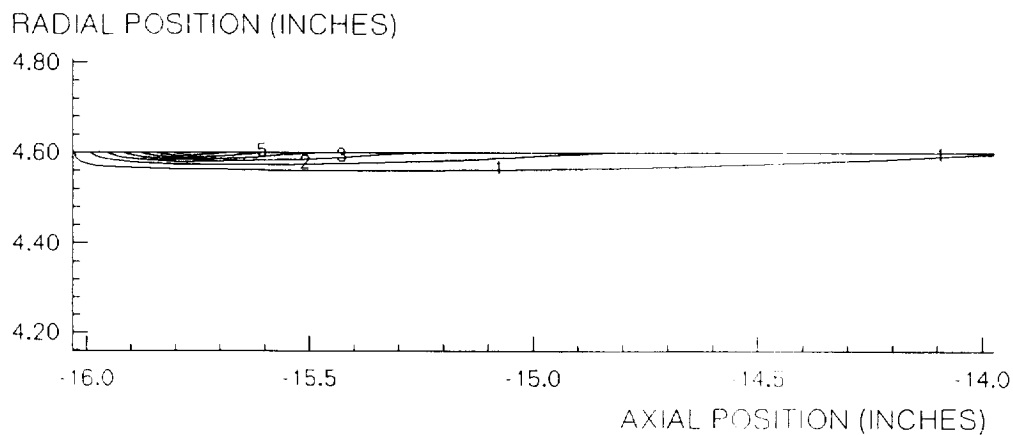


Figure 3.6:  $C_6H_6$  Mass Fractions at the Injector for the Downstream Port Film-Cooling Case

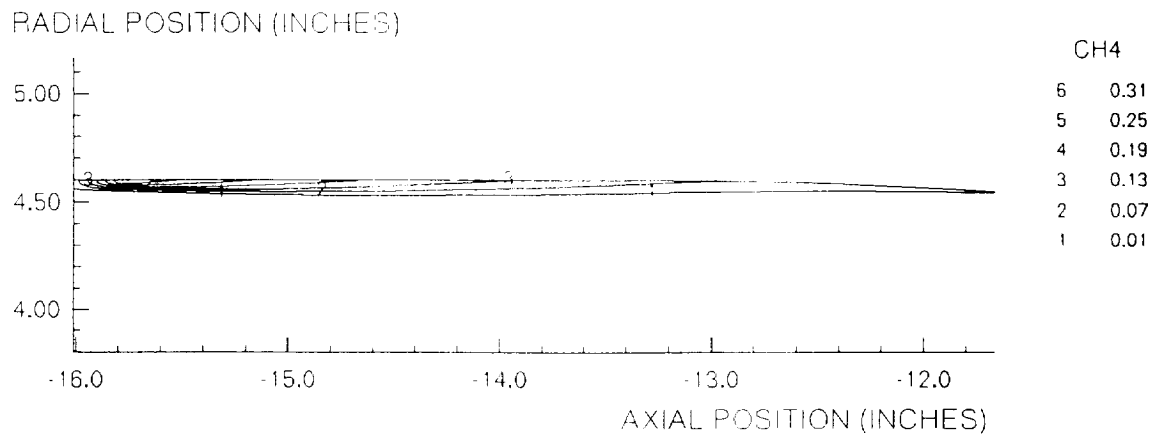


Figure 3.7: CH<sub>4</sub> Mass Fractions at the Injector for the Downstream Port Film-Cooling Case

(Figure 3.5). Benzene exists down to an axial position of -14 inches (Figure 3.6). Figure 3.7 shows that the reach of methane extends to an axial position of -11.6 inches. From the nozzle wall temperature distribution for film-cooling at the injector face and at the downstream port, shown in Figure 3.1, a significant increase in the axial temperature gradient along the nozzle wall occurs at an axial position of -11.5 inches. This again correlates with the farthest extent of methane during the RP-1 cracking process.

Figures 3.8, 3.9, and 3.10 are contour plots of the mass fractions of RP-1, C<sub>6</sub>H<sub>6</sub>, and CH<sub>4</sub>, respectively, at the downstream port for case 3. The port lip ends at -8 inches and the coolant is exposed to the hot core gases. The gaseous RP-1 quickly breaks down in the first 0.5 inches past the port lip (Figure 3.8). Benzene exists down to an axial position of -5 inches (Figure 3.9). Figure 3.10 shows that the reach of methane extends almost to the throat. From the nozzle wall temperature distribution for film-cooling at the injector face and at the downstream port, shown in Figure 3.1, the wall temperature temporarily decreases during the thermal expansion of the flow in the throat region. Then, a significant increase in the axial temperature gradient along the nozzle



wall occurs just downstream of the throat. This seems to further correlate the coolant effectiveness with the farthest extent of methane during the RP-1 cracking process.

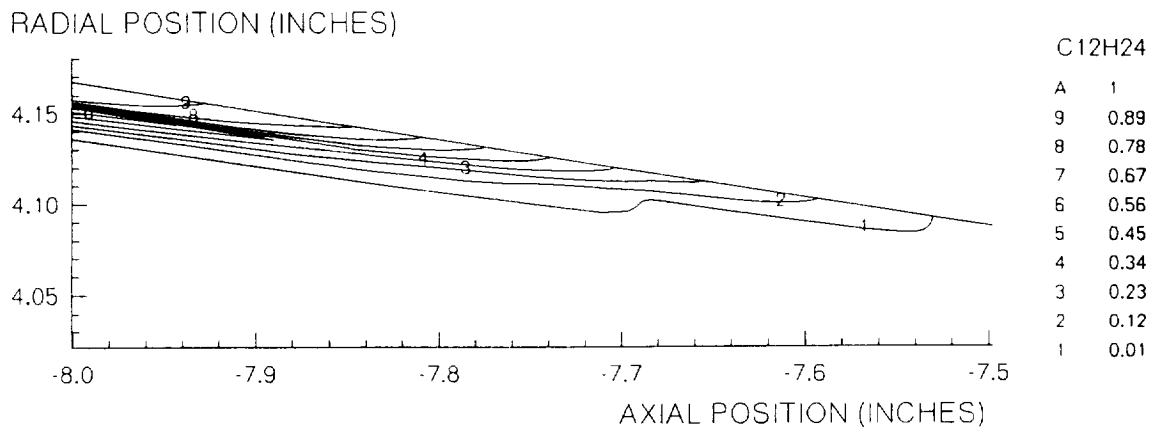


Figure 3.8: RP-1 Mass Fractions at the Port for the Downstream Port Film-Cooling Case

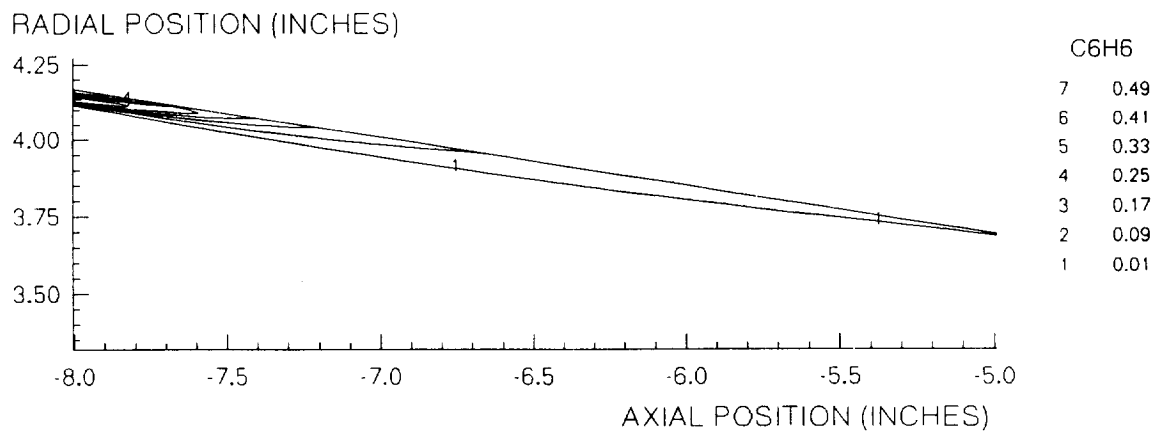


Figure 3.9: C<sub>6</sub>H<sub>6</sub> Mass Fractions at the Port for the Downstream Port Film-Cooling Case

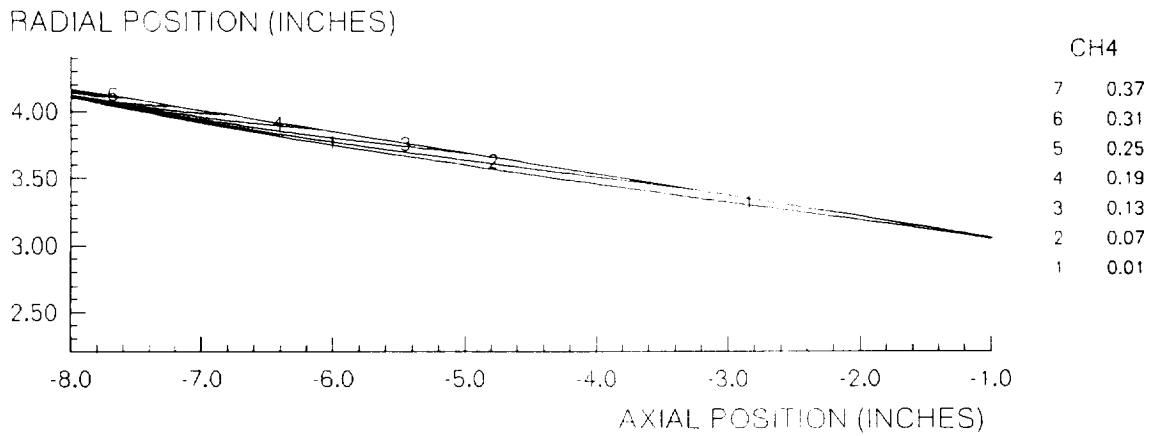


Figure 3.10: CH<sub>4</sub> Mass Fractions at the Port for the Downstream Port Film-Cooling Case

### 3.3. Survivability of the Copper Lip

The predicted temperature distribution in the copper lip of the downstream coolant port is shown in Figure 3.11. The temperature of the copper lip varies between approximately 2220°R and 2340°R. Since the melting point of pure copper is approximately 2440°R, it appears that the copper lip will indeed survive in this environment with this particular coolant flowrate without melting. However, if the numerical uncertainty in the calculated temperatures of the copper lip is greater than 100°R, or if the design margin of safety in temperature is greater than 100°R, then a copper lip may not be acceptable. Also, if the coolant port design differs significantly from the one analyzed in this study or if the coolant flowrate is reduced, there could be localized hot spots which are hot enough for the copper to melt. This result requires further verification.

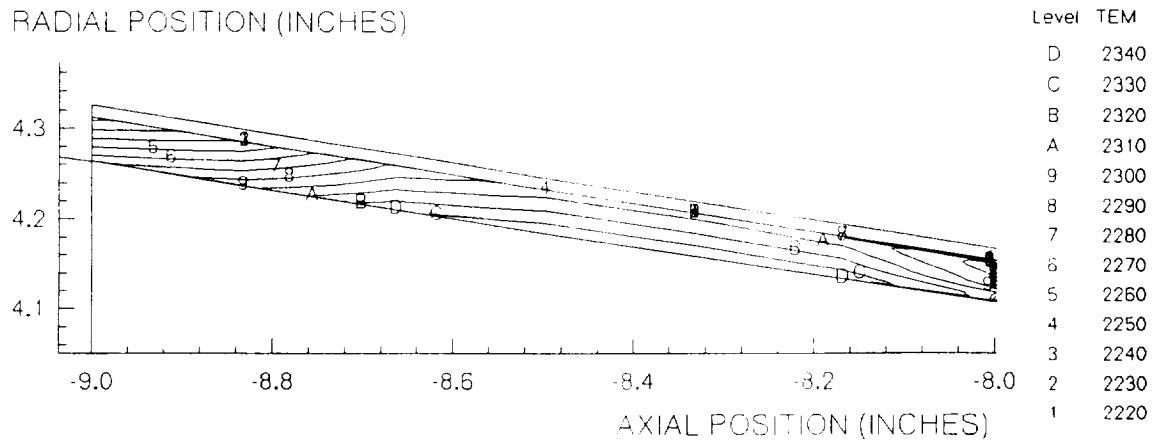


Figure 3.11: Temperature Distribution in the Copper Lip

### 3.4. Performance Comparison

Table 3.1 summarizes the performance ( $I_{sp}$ ) of the three nozzle cases simulated. Film-cooling with 10% of the fuel flowrate results in about a 2% decrease in performance from the maximum performance attainable when no film-cooling is used. The nozzle performance is not significantly effected by the redistribution of some of the coolant to the additional downstream port.

Table 3.1: Nozzle Performance Comparison

Nozzle Simulation Case	$I_{sp}$
No Film-Cooling	263 sec
Film-Cooling at the Injector	258 sec
Film-Cooling at the Injector and at a Downstream Port	257 sec

## IV. CONCLUSIONS

The objective of this research effort was to evaluate the impact of incorporating an additional coolant port downstream between the injector and nozzle throat in the NASA Fast Track chamber. A numerical model of the chamber was developed for the analysis. This analysis did not model ablation but instead correlated the initial ablation rate with the initial nozzle wall temperature distribution. The results of this study provide guidance in the development of a potentially lighter, second generation ablative rocket nozzle which maintains desired performance levels.

There are four main conclusions that can be drawn from this work. First, it appears possible to optimize the distribution of film-coolant between the injector and the additional coolant port to bring the entire nozzle wall temperature distribution down below the 3600°R threshold temperature for maintaining the ablation rate of the nozzle liner below 2 mils/sec. However, adding another coolant port to the nozzle significantly increases the complexity and cost of the nozzle design. The current study results indicate that simply adding slightly more coolant massflow at the injector face could drop the wall temperature to acceptable levels, if acceptable performance can be maintained. Second, the cooling effectiveness of RP-1 seems to be primarily due to a highly endothermic cracking process. Third, it appears that with reasonable coolant flowrates, the additional coolant port could potentially be manufactured out of inexpensive copper. Finally, nozzle performance was only marginally diminished (2%  $I_{sp}$  decrease) by the use of film-cooling in the LOX/RP-1 rocket.

Although the ablation rate of the silica-phenolic nozzle liner was originally considered to be the biggest obstacle to the viability of this simple, low cost rocket nozzle, test firings of the NASA MSFC Fast Track engine have indicated that there is no net change in the thickness of the nozzle in the throat region because the ablation rate of the nozzle liner appears to be balanced by an equivalent rate of coking.<sup>10</sup> This layer of deposited carbon effectively acts as an insulative

layer to help protect the silica-phenolic liner from the harsh temperatures of the surrounding flow of hot gases. The occurrence of coking is not surprising based on the results of this numerical research. Coking is a kinetically-controlled process which occurs over a specific range of very lean mixture ratios and temperatures. The numerical predictions indicate that the flow next to the wall in the throat region is oxygen lean and at the right temperatures for coking to occur. Also, any carbon that is formed just upstream of the throat in the converging section will likely be deposited on the nozzle wall in the throat area.

## V. FUTURE WORK

Additional simulations of the NASA Fast Track nozzle with film-cooling both at the injector and at the additional downstream coolant port are planned. In these simulations, the coolant flowrates and port location will be varied in an attempt to obtain a more uniform nozzle wall temperature distribution and thus ablation rate for the silica-phenolic nozzle liner. Simulations of the nozzle at various chamber pressures will also be performed. Benchmarking the numerical predictions with available experimental data will also be a priority. Any useful results obtained from this future work will be submitted to NASA MSFC as an addendum to this research report.

## REFERENCES

1. Aerojet-General Corporation. Technical Report. 1969.
2. CFD-ACE Theory Manual. CFD Research Corporation. Huntsville, Alabama. 1993.
3. Ten-See Wang. NASA MSFC (ED32). Private Communication. 1995.
4. "TEP for Windows: A Combustion Analysis Tool -- Version 1.0 User's Manual." Software and Engineering Associates, Inc. 1994.
5. "Estimated Viscosities and Thermal Conductivities of Gases at High Temperatures." Roger Svehla. NASA TR-R-132. NASA Lewis Research Center. Cleveland, Ohio. 1962.
6. *Transport Phenomena*. Bird, Stewart, and Lightfoot. Wiley. New York, NY. 1960.
7. CPIA/M4 Liquid Propellant Manual. 1966.
8. *Handbook of Viscosity*. Carl Yaws. Gulf Publishing Co. Houston, TX. 1995.
9. *Fundamentals of Heat and Mass Transfer*. Frank Incropera and David DeWitt. Wiley. New York, NY. 1990.
10. Warren Peters. NASA MSFC. Private Communication. October 1995.